Laminar Separation Bubble Dynamics and its Effects on Thin Airfoil Performance During Pitching-up Motion

Zhaolin Chen[a] , Tianhang Xiao[a], Yan Wang[a], and Ning Qin[b]

Abstract

This paper reports an investigation into dynamic characteristics of the laminar separation bubbles (LSBs) associated with aerodynamic loads unsteadiness of a cambered-thin airfoil in pitching-up motions at low Reynolds number flows. Unsteady Reynolds Averaged Navier-Stokes (URANS) simulations were conducted for a 4%c cambered-thin airfoil at Reynolds number of 30,000 and 60,000. The airfoil pitches up from $0°$ to $25°$ angles of attack at dimensionless pitch rate $\dot{\alpha}$ of 0.0398 and 0.0199. The $k - \omega$ SST $\gamma - \tilde{R}e_{\theta t}$ turbulence-transition model was used to account for the effect of transition on LSBs development. The LSBs show are shown to evolve in their shape and size during the pitching motion. The influence of the LSBs on the airfoilupper surface during pitching motion continues to a higher incidence in comparison with that under static conditions before developing into a fully detached flow. Vortex merging is observed in the rear-part of the LSBs in the turbulent portion for a Reynolds number of 30,000. At Reynolds number 60,000, the changing of the laminar separation bubble length during pitching-up motion is similar to that of steady cases, except a delayed transition is observed as incidence increases. The results show further insight into the dynamic characteristics of the laminar separation bubbles and their relation to the airfoil's aerodynamic performance. Not better.

[a] Department of Aircraft Design, College of Aerospace Engineering, Nanjing University of Aeronautics and Astronautics, Nanjing, China
[b] Department of Mechanical Engineering, University of Sheffield, Sheffield, UK

Corresponding author:
Zhaolin Chen, College of Aerospace Engineering, Nanjing University of Aeronautics and Astronautics, 29 Yudao Street, Nanjing, 210016, People's Republic of China.
Email: zhaolin_chen@nuaa.edu.cn

1. Introduction

Laminar boundary-layer separation occurs due to a strong adverse pressure gradient, followed by the laminar-turbulent transition in a detached shear layer. The turbulent shear flow eventually re-attaches downstream, and then a closed bubble is formed. A detailed introductions to laminar separation bubbles (LSBs, see Figure 1) was given by Gaster M (1969)[1]. LSBs appear in numerous aerodynamic applications, such as dynamic stall characteristics of wings, rotary blades[2], low-Reynolds-number flying vehicles, high-altitude long-endurance unmanned aerial vehicles (HALE-UAVs)[3], Mars exploration aerial vehicles[4], and wind turbines with enhanced laminarity[5]. The applications described above share a closely related common problem in understanding low Reynolds number aerodynamics[6].

A better understanding of aerodynamic characteristics at low-Reynolds-numbers is important for the development of such aerodynamic applications. For pitching airfoils at low Reynolds Numbers, 10,000 < Re_c < 500,000, the flow field has a strong unsteady and viscous effect, leading to a complex transient vortical flow, in which a unique phenomenon is the formation of laminar separation bubbles. It is well-known that the laminar boundary layer can only sustain a small amount of adverse pressure gradient. Thus, encountering a strong adverse pressure gradient near the leading-edge, the boundary layer is susceptible to laminar flow separation. Dovgal et al. [7] pointed out that the Kelvin–Helmholtz instability of the separated shear layer amplifies the small-amplitude disturbances exponentially, leading to boundary layer transition. Lambert and Yarusevych[8] proposed a mechanism for understanding the vortex dynamics inside the LSBs. They mentioned that amplified disturbances cause the separated shear layer to roll up and form discrete vortices. Michelis et al.[9] pointed out that these vortices are convected along with the separation bubble and promote the re-attachment of the mean flow. The development and interaction of these vortex structures are essential to transitional and turbulent shear-layer development.
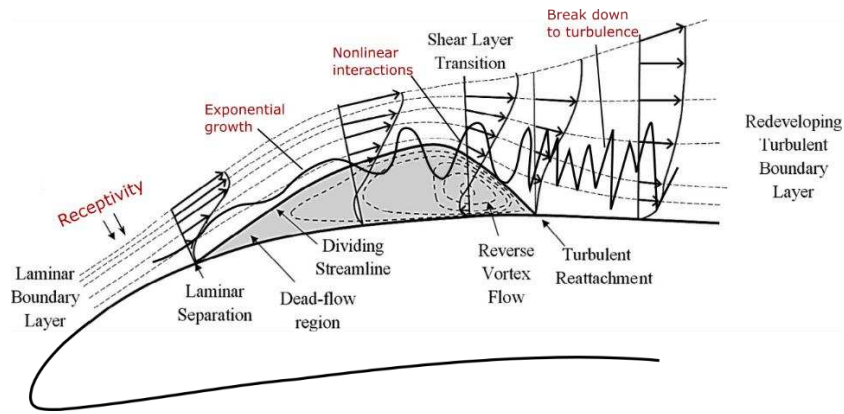
Figure 1 The mean flow structure of a laminar separation bubble

Airfoil performance is sensitive to separation, transition and reattachment, which is closely related to the dynamic characteristics of LSBs. Therefore, the influence of LSBs on airfoil performance and the associated flow phenomena have been the focus of substantial research. Early research on the time-averaged characteristics of LSBs on airfoil and plate were carried experimentally by Tani [10] and Horton[11]. The definition of 'short' and 'long' bubbles was given by Gaster[1]. Later research on laminar boundary separation and associated phenomena were! carried out by Westini et al.[12], O'Meara, and Mueller[13]. More recently, DeMauro et al.[14] and Rinoie et al.[15] conducted an experimental investigation on dynamic characteristics of LSBs with a control mechanism involved. Sudhakar et al.[16] conducted an experimental study on the effect of leading-edge tubercles on the LSBs using particle image velocimetry. To handle the separation-induced transitional flow, turbulence models with specific transition prediction Reynolds-averaged Navier-Stokes (RANS) need to be integrated. Lee and Nonomura et al.[17] conduced numerical studies on the prediction of aerodynamic characteristics derived from three numerical methods at various Reynolds numbers, including laminar, Baldwin-Lomax turbulence model, and three-dimensional large-eddy simulations. The results from both 2-D laminar and 3-D LES simulations shown some validated airfoil aerodynamic characteristics. However, the 2-D RANS with Baldwin-Lomax turbulence model simulation could not capture the nonlinearity of C_L. This problem (non-linear lift?) may be attributed to the use of a full turbulence model with a fixed transition point in their 2-D RANS simulation. Bernardos

et al.[18] developed an algebraic transitional extension of $k - \omega$ model for the accurate computation of laminar separation bubbles. The transition modeling formulation account for progressive turbulence growth within LSBs, and the results highlighted the improvement over classical RANS approaches.

On the other hand, correlation-based models have widely integrated with transition correlations into coefficients of transport equations for the intermittency. The RANS with $\gamma - \tilde{R}e_{\theta t}$ transition model[19] uses transport equations for the intermittency and the momentum thickness Reynolds number. It was developed based on local variables, which are valid for both natural and bypass transition in boundary layers with and without pressure gradient[20] and represents a very promising strategy. Dick and Kubacki[21] summarized the distinction between algebraic (intermittency) models and transport (intermittency) models. With a transport model, the intermittent is obtained by the spatial-temporal differential equations representing convection, diffusion, production and, dissipation, similar to the transport equations for turbulence models. The onset and growth of intermittency may be derived from correlations, where various methods on determination of the integral parameters in the correlations can be implemented. Liu, J., and Xiao, Z. et al.[22] investigated the unsteady transition over an oscillating airfoil through the three-equation k-ω-γ transition model. Their results have shown that the dynamic pitching derivatives of transitional flows are sensitive to the reduced frequency and increases linearly. A detailed study on dynamic stall using turbulent-transition model URANS was also conducted by Geng et al.[23]. The simulation results showed that the lift coefficient benefited from the transition model is more accurate for the transition modeling approach. The simulation also confirmed that during the pitching-down movement, the aerodynamic forces were much more sensitive to changes in the computational parameters than what is compared? as compared with the pitching-up movement. Their numerical results also showed that turbulence models and grids resolution are essential parameters for obtaining accurate simulation results. The grid first cell height, the computational time step size, and the airfoil trailing-edge geometry (sharp or blunt) in the simulations are investigated and shown to be comparatively less critical factors.

In the above studies, the LSBs on relatively thick airfoils are investigated. The LSBs form near the trailing-edge and moves towards the leading-edge as the incidence increases[24]. For thin airfoils, the LSBs developed near the leading-edge and interacted with trailing-edge separation shown in our earlier paper[25], and the nonlinear lift was also predicted at moderate incidences for both 2D and 3D cases. Since the dynamic behavior of LSBs for a thin airfoil in dynamic pitching motion is still unknown, and it is the focus of this work.

The current investigation aims to gain further insight into the development of the laminar separation bubble for a pitching airfoil, affecting overall aerodynamic performance. The pitching center is at the quarter chord location downstream of the leading-edge, as depicted in Figure 2. The Reynolds numbers are 30,000 and 60,000 for both fixed and pitching-up motion. Laminar separation, laminar-turbulent transition, reattachment, aerodynamic forces evolution, and flow pattern development during the pitching motions are analyzed and detailed.

2. Computational framework

2.1 Governing equations and solution details

All simulations were performed with the ANSYS/FLUENT software using finite volume incompressible Reynolds-averaged Navier–Stokes solutions coupled with a transition model and a turbulence model. The moving mesh integrated over a control volume is coupled with continuity and momentum equations. For clarity, the following shows the mathematical models:

$$\frac{\partial}{\partial t}\int_{V_c} \rho^f \, dV_c + \oint_S \rho^f(\boldsymbol{v}-\boldsymbol{v_g})\cdot \mathbf{n}\, dS = 0 \tag{1}$$

$$\frac{\partial}{\partial t}\int_{V_c} \rho^f \boldsymbol{v}\, dV_c + \oint_S \rho^f\boldsymbol{v}(\boldsymbol{v}-\boldsymbol{v_g})\cdot \mathbf{n}\, dS = -\oint_S \boldsymbol{\tau}\cdot \mathbf{n}\, dS - \oint_S \mathrm{p}\cdot \mathbf{n}\, dS \tag{2}$$

where, ρ^f is the fluid density, $\boldsymbol{v}$ is the fluid velocity vector which is based on the Cartesian coordinates, $\boldsymbol{v_g}$ is the moving grid velocity, $\boldsymbol{\tau}$ is the molecular momentum transport tensor, and p indicates the pressure

gradients term, V_c is the mesh cell control volume, **n** is the normal vector to the control volume surface, and **S** is the control volume surface area.

Reynolds Averaged Navier–Stokes (RANS) with fully turbulent modeling is not appropriate for transitional flows[26]. Low-Reynolds-number turbulence models are capable of resolving the viscous sublayer, such as the $k - \omega$ low Reynolds number model, normally with either under- or over-predicted transition or reattachment locations for the case of LSBs occurring[27]. While for tripping or forcing an early/delayed transition occurrence, ignoring ???transition physicscan cause the solution to be unreliable. Intermittency with empirical factor-based models shows satisfactory and cost-effective solutions on transition prediction. However, a limitation on two dimensional and nonlocal parameters generally are confined to bypass transition modeling. The $\gamma - \widetilde{R}e_{\theta t}$ transition model of Menter et al.[28] that couples the SST model with transport equations for the intermittency and Re_{θ} (i.e., momentum-thickness Reynolds number). The significant improvement of this transition model is that it is not relying on nonlocal parameters. Hence it is more suitable for modern CFD codes and complicated transitional-flow simulations. Besides don't start with besite A special modification to the intermittency is included to allow for separation-induced transition prediction. This paper adopts the transition model, which is proportional to the maximum strain-rate Reynolds number. The vorticity Reynolds number (Re_v) is defined as:

$$Re_v = \frac{\rho y^2}{\mu} \frac{\partial u}{\partial y} = \frac{\rho y^2}{\mu} \Omega \tag{3}$$

No the for notations Ω and y, in(3), are the vorticity and the wall-normal distance, respectively, and the maximum value of Re_v is dependent on the Re_{θ}. The momentum-thickness Reynolds-number transport equation is used to capture the nonlocal effect of freestream-turbulence intensity and pressure gradient at the boundary-layer edge, which indicates where transition onset occurs, and defined as:

$$\frac{\partial(\rho \widetilde{R}e_{\theta t})}{\partial t} + \frac{\partial(\rho U_j \widetilde{R}e_{\theta t})}{\partial x_j} = P_{\theta t} + \frac{\partial}{\partial x_j}\left[\sigma_{\theta t}(\mu + \mu_t)\frac{\partial \widetilde{R}e_{\theta t}}{\partial x_j}\right] \tag{4}$$

The transport equation for intermittency is used to trigger the transition process ($\gamma > 0$) and is defined as:

$$\frac{\partial(\rho\gamma)}{\partial t} + \frac{\partial(\rho U_j\gamma)}{\partial x_j} = P_\gamma - E_\gamma + \frac{\partial}{\partial x_j}\left[\left(\mu + \frac{\mu_t}{\sigma_f}\right)\frac{\partial\gamma}{\partial x_j}\right] \qquad (5)$$

However, when the boundary separates, the modification of intermittency to one, and defined as:

$$\gamma_{sep} = min\left\{8\,max\left[\left(\frac{Re_v}{2.193Re_{\theta c}}\right) - 1, 0\right]e^{-\left(\frac{R_T}{15}\right)^4}, 5\right\}F_{\theta t} \qquad (6)$$

In the above equations, Eq. (5) and (6), F_{length} and $Re_{\theta c}$ are two key functions, in which the former controls the transition extent, and the latter determines the onset of transition. The source term P_γ will be activated when the local strain-rate Reynolds number exceeds the local transition-onset criterion. The destruction source term E_γ enables relaminarization prediction when the transition-onset criterion is no longer satisfied and vanishes in the fully turbulent regime. A complete description of the model is available in the article by Menter et al.[28]

2.2 Geometry details and computational methodology

A cambered plate airfoil with a thickness-to-chord ratio of 1.93% was designed to have a 5-to-1 elliptical leading-edge, and a 3° sharp trailing-edge is shown in Figure 2(a)[25]. The present investigation of a thin airfoil performed in pitching motions about the quarter chord location with dimensionless pitch rate $\dot\alpha$. Detailed parameter specifications of the present numerical investigation are listed in Table 1.

Table 1 Details of investigation cases: boundary conditions and model parameters

Airfoil	Cambered-thin airfoil
Chord length, c (m)	0.1
Chord Reynolds number, Re_c	3×10^4 and 6×10^4
Dimensionless pitch rate, $\dot\alpha = \frac{\omega c}{U_\infty}$	0.0398 and 0.0199
Free stream turbulent intensity, T_i	0.05%

Variation of incidence , α (°)	From $0°$ to $25°$
Trailing-edge shape	Blunted, shown in Figure 2 (c)

Figure 2 (c) shows a general view of the structured mesh topology for the 2D thin airfoil geometries for the present study. Based on the mesh sensitivity analysis results change back. Bad to use too many nouns as adjectives. from our previous study[25], the same mesh topology but with a different grid level is applied for the present investigations. A dense grid in the boundary layer, especially around airfoil leading- and trailing-edge, is utilized to capture the boundary layer separation with y+ superscript + value in the order of one. The O-grid mesh topology was applied for the rotational domain, and the edge expansion ratio in the normal direction was set to 1.2 to ensure a smooth mesh with 50 grid points inside the boundary layer, shown in Figure 2 (b). Grid orthogonality was also maintained on the wall surface to make a high-quality quadrilateral mesh element along the airfoil surface. The sliding mesh technique was applied on the interface between the rotational and stationary domain, and a quadrilateral mesh element with an aspect ratio of 1~1.3 was strictly constrained on the interface boundary[23].

All computational cases were split into two sub-steps. A steady-state solver is used to initialize the flow field at an incidence of 0° why plural? . Based on the steady-state flow solution as a starting point, the airfoil's dynamic pitching motion will be activated by a moving grid simulation, in which the sliding mesh technique is employed to couple the rotational and stationary domains. The time step was set sufficiently small to capture the flow features, including the LSBs development process of the dynamic loading acting on the airfoil. The resolving time has 5000-time steps with about 20 inner iterations per time step to complete one pitching-up motion with a corresponding time step value of $\Delta t = 1 \times 10^{-4}$s. The simulation terminates when the cyclic forces are converged.

For boundary conditions, pressure, incoming freestream velocity, freestream turbulent intensity, and the turbulence length scale are imposed at the inlet, with pressure prescribed at the outlet boundary.

Furthermore, the non-slip boundary condition is applied on the airfoil surface. The turbulent kinetic energy is set to zero at the wall, and the pressure on the wall has zero normal gradients.
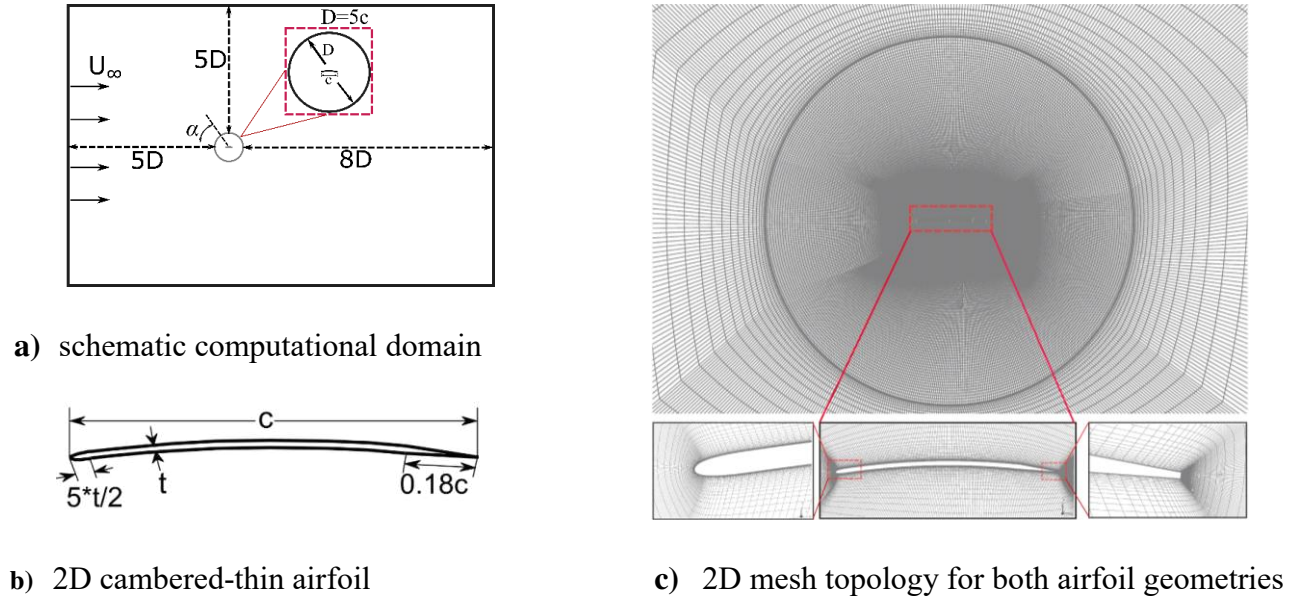

a) schematic computational domain

b) 2D cambered-thin airfoil

c) 2D mesh topology for both airfoil geometries

Figure 2: Airfoil geometry and mesh

2.3 Validation case

A detailed pitching-motion two-dimensional aerofoil case by LEE[29] as an original investigator, followed by further validation and verification works by Kim[30], Wang[31], Gharali[32], and Geng[23], has been chosen to verify our present numerical methods. Wind tunnel measurements were taken for NACA 0012 aerofoil with pitching motion to investigate the unsteady boundary layer and stall events. Aerofoil has a chord length of 0.15m and a 2.5c span mounted horizontally in the 0.9m (height) × 1.2m (width) × 2.7m (length) suction-type wind tunnel at McGill University, Canada. Two wing-tip plates with a diameter of 2c were installed at the ends of the wing to minimize the cross-flow due to the wing-tip effect, hence eliminating the effect of highly unsteady swirls at the aerofoil edges. The blockage ratio was 2.2% which was based on the aerofoil at its maximum AoAs ($\alpha = 25°$). The Reynolds number was Re = 135,000 based on the chord length and freestream velocity U_∞. The pitching motion is described using the angle of attack $\alpha(t) = 10° + 15° \sin(\omega t)$, and the pitching axis is at the quarter chord point from the leading edge.

The corresponding reduced frequency k was 0.1 in this study. The computational domain is set by an upstream and downstream distance of 10c and 20c, respectively. The upper and lower distance set at 10c away. Symmetric boundary conditions were applied on the two lateral boundaries. Arguably the simulations of a pitching airfoil are less sensitive than those of a static airfoil. A semi three-dimensional wing with an extension of 0.2c in spanwise direction is designed to study the 3D effect under the pitching motion. Barnes, C. J., and Visbal, M. R.[33] pointed out that the spanwise extension of 0.2c is sufficiently wide to capture the spatial evolution of flow features.

Due to the computational cost, mesh sensitivity studies are firstly performed for two-dimensional cases. Secondly, the appropriate 3D mesh size for NACA0012 pitching-motion is implemented through the analysis of the two-dimensional results. Finally, both 2D and 3D results are compared with the experimental data. The present computational simulations use an O-type mesh around the aerofoil with the same boundary layer mesh strategy, as shown in Figure 2 (c). Three sets of different 2D grids were employed in order to explore the effect of spatial resolution. To facilitate this assessment, some details of the various meshes, denoted as coarse (G1), median (G2), and fine mesh (G3), are summarized in Table 1. For grids G1 and G2 the streamwise mesh resolution increases while retaining the same spacing for the normal direction. However, G2 and G3 remain the same mesh resolution in a streamwise direction and increases the normal spacing with a doubled grid value of G2.

The comparison of experimental and computed aerodynamic loads, averaged from three pitching cycles, are shown in Figure 3, and the main interest in dynamic stall phenomena is the load variation between pitching motions. In general, it can be seen that the computed aerodynamic loads using all three 2D mesh grids, G1, G2, and G3, follow the trend of the experimental data well during the upstroke phase when the flow field is attached to the airfoil surface. The results from grid G1 differ from G2, and G3 mainly in the peak C_l region. However, local discrepancies are observed from all grids in the downstroke phase due to the complex post-stall process in the flow. Figure 3 shows a good C_l comparison results from G1 to G3, particularly for the upstroke phase when the flow is attached, and noticeable differences but

good trend are observed between G2 and G3 during the downstroke. Due to the expensive computational demand, we take the view that the solutions obtained from G2 are acceptable, and thus G2 was chosen as the base for the three-dimensional grid G4.

The force comparison why do you link two nouns here? shows some discrepancies between 3D numerical results (noted as G4) and wind tunnel data. Both 2D and 3D numerical models show conspicuous oscillations of the lift curve with respect to the experimental data force. The flow field is characterized by the formation of strong vortices moving on the airfoil's upper surface during the downstroke motion. A fair agreement between the experimental and numerical is observed during the upstroke motion for 3D simulation at C_L peak value, as shown in Figure 3. The two-dimensional results, based on aerodynamic coefficient analysis, are in good agreement with the experimental values. Besides this, at 10° angles of attack, the transition locations obtained by 2D and 3D simulations are also quite comparable with experimental values. Therefore, the results obtained using two-dimensional simulations (e.g., G3 mesh size) are presented in the following part of this paper.
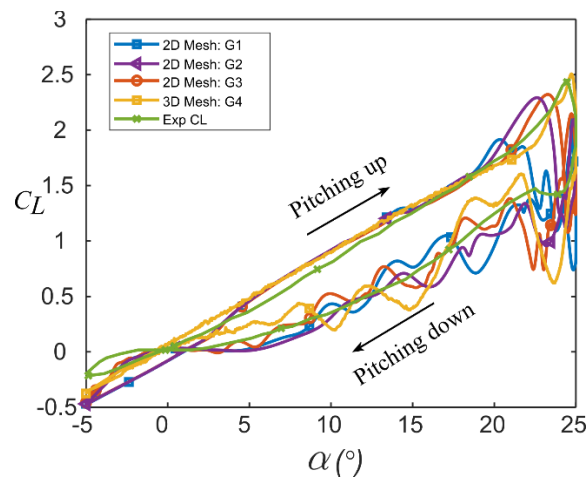

Figure 3 Grid sensitivity study on a NACA0012 pitching-motion validation case: lift coefficient C_L variation with one pitching cycle

Table 2 Grid-sensitivity at α = 10°

Grid	Size	$C_{l, upstroke}$	$C_{l, downstroke}$	$C_{d, upstroke}$	$C_{d,downstroke}$	$x_{tr}/c_{, upstroke}$
G1 (2D)	340×235	0.9138	0.5241	0.0762	0.1059	0.1028
G2 (2D)	680×235	0.9031	0.3342	0.0758	0.1141	0.1172
G3 (2D)	680×470	0.9157	0.3162	0.0763	0.0850	0.1324
G4 (3D)	680×235×40	0.8937	0.2104	0.0731	0.0452	0.1031
Experiment		0.8053	0.3059	0.0932	0.0608	0.1279

3. Results and discussion

For this section, numerical results for laminar separation bubble evolution against changing angles of attack are discussed in detail. Before investigating the dynamic effects of pitching motion on laminar separation formation and development, the characteristics of the LSBs on a fixed airfoil are first investigated here.

3.1 Laminar separation bubbles for a fixed airfoil at different incidences for Re=30000 and 60000

In this section, the mean flow characteristics are analyzed, the time-averaged separation, transition, and reattachment location, x_{sep}/c, x_{tr}/c, and $x_{reattch}/c$, are found at each incidence for the fixed airfoil. The separation and reattachment locations in Figure 4 were obtained by determining the zero crossings of the skin-friction coefficient[34]. The separation, transition, and reattachment loci are discussed in section 3.2.2, shown in Figure 10 (a and b) for Reynolds numbers at 30,000 and 60,000, respectively.

In the fixed airfoil case, the similarities of separation bubble characteristics can still be found at the two different Reynolds numbers. The most obvious is that the separation bubble lengthens as the incidence rises, moving the transition location toward the leading-edge and the reattachment point toward the trailing-edge. As expected, the separation bubble moves upstream as the magnitude of the adverse pressure gradient downstream of the suction peak increases with increasing angle of attack. The front portion of

the bubble, the region between separation and transition shown in Figure 5, has a significant shrinkage process as the Reynolds number increases from 30,000 to 60,000. The possible reason is the increase of adverse pressure gradient, causing early transition to turbulent, quicker pressure recovery, stronger shear as presented by the increasing skin friction value (C_f) on suction surface, hence leading to early reattachment. These trends were also observed by Counsil and Boulama[26], Lian and Shyy[35], and Lei et al.[36].

At low angles of attack, 4° and 5°, fully attached flow with a limited separation region at the trailing-edge area is found for Reynolds number of 30,000. Whereas, at 5° of incidence, the distribution of skin friction coefficient shows a tiny informal English. What is tiny? Very small is better in technical sense. bubble, whose influence can be ignored as no pressure plateau is shown in Figure 4 (b and c, 5° dashed orange line). Nevertheless, the flow in the wake region for both angles of attack remains smooth. At incidences of 6° and 7°, the characteristics of LSBs are similar, but the apparent same difference lies in the laminar and turbulent portions of the bubble, as shown in Figure 4 (b and d, the intermittency contour). An intermittency value of zero indicates laminar flow, whereas a value of 1 indicates a fully turbulent flow. The upper surface flow original is better English is laminar, which through a separation bubble, reattaches, and transitions to a turbulent flow. The lower surface remains laminar for much of its chord length. The freestream value of 1 is a result of the fully turbulent SST model being used in the freestream. In contrast, a bubble with 30% of chord length is observed on the upper surface at the incidences of 6° and 7° at Reynolds number at 30,000 in Figure 4(f, purple line), whereas a shorter bubble with 20% of chord length has been found on the upper surface at the Reynolds number is 60,000.

By observing the categories of the flow region in Figure 4 (a, b), the following conclusions can be drawn. At low incidences (0° to 4°), the attached flow occupies between 70 and 80% of the chord length, and separation with a limited area is observed in the airfoil's trailing-edge change back to better English. At moderate angles of attack (about 4° to 8°), separation bubbles start to form on the airfoil surface, and

different Reynolds numbers show incorrect. What other? Change back characteristics of separation bubbles. At Reynolds number 30,000, the separation bubbles are or are getting long longer? we do mean longer here. What is long? For both?, with the length reaching 50% chord at 8° incidence. While at Reynolds number 60,000, the most extended size of separation bubbles is about three-fifth 3/5 no plural of the former (found at 8° angles of attack). The most obvious is the flow reattachment area (the dark green region in Figure 4), which increases with the rise of Reynolds number. Compared with the Reynolds number of 30,000, the incidence rose, and the transition location moved towards the airfoil leading-edge at 60,000 more significantly. At high angles of attack (α > 8°), the separation bubble burst, and fully detached flow forms on the airfoil surface, as shown in Figure 4.

a) Vorticity Magnitude   b) Intermittency   c) Cp distribution   d) Cf distribution

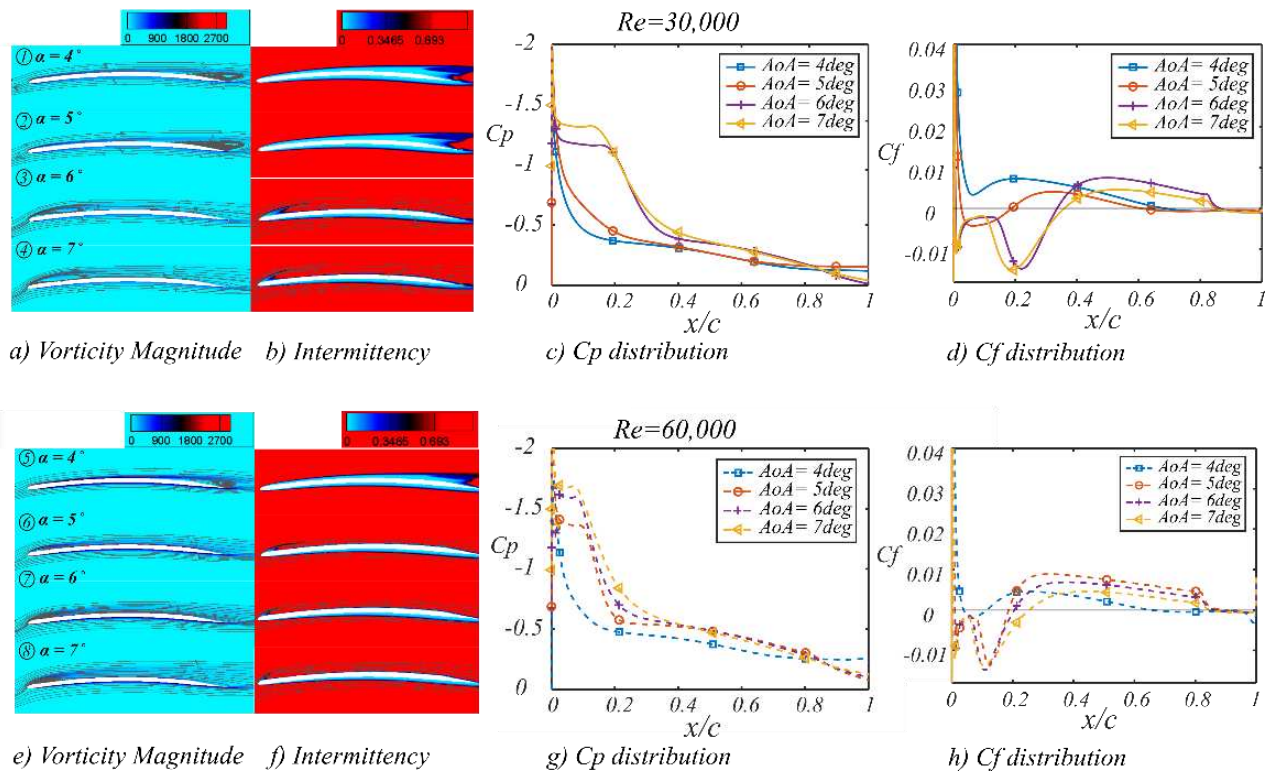e) Vorticity Magnitude   f) Intermittency   g) Cp distribution   h) Cf distribution

Figure 4 Time-averaged contour of vorticity magnitude, intermittency, and suction-surface C_P, C_f distributions for the fixed cambered-thin airfoil
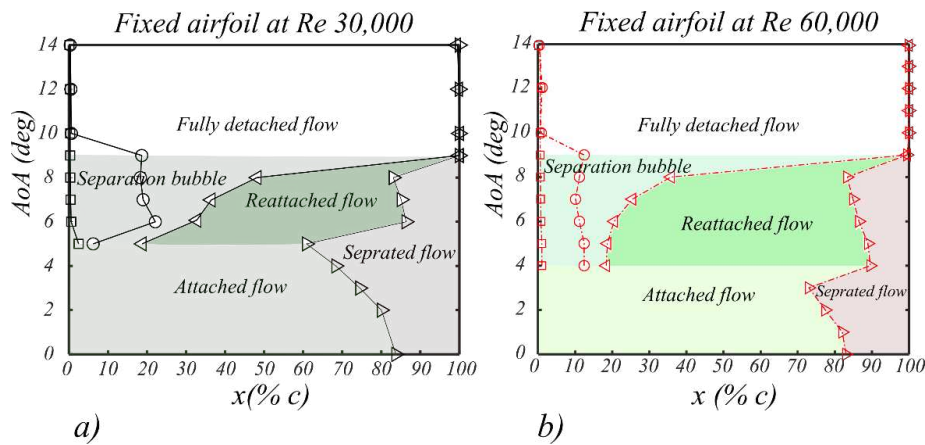
Figure 5 Characteristic bubble parameters for fixed airfoil, laminar separation loci: (—□—); transition loci: (—○—); reattachment loci: (—◁—); trailing-edge separation loci: (—▷—)

3.2 Laminar separation bubble development during airfoil pitching motion at two different Reynolds numbers

3.2.1 Aerodynamic loading characteristics

Figure 6 and Figure 8 show the averaged aerodynamic loads for pitching-up motion at Reynolds numbers of 30,000 and 60,000, respectively. The solid and dash line indicate the lift and drag coefficient in pitching-up motion respectively. The aerodynamic loading of the pitching-up motion rises smoothly for both Reynolds numbers throughout the rest of the maneuver, with the most significant deviations appearing in the oscillations in the lift /drag coefficients at low and moderate incidences.

The lift coefficient rises smoothly for pitching-up motion at Reynolds number 30,000, except for low (around 1°) and moderate (between 10° and 13°) angles of attack. The lift-curve for steady case (with circular hollow markers), on the other hand, started with a sudden jump at 5° (i.e., the formation of short LSBs) and followed with a C_l-dropping at 10° incidence (i.e., short bubble burst to form a long bubble). Such a laminar separation bubble formation and progress versus angles of attack can be found in Figure 5(a).

The streamwise vortex resulting in the formation process is most clearly visible in Figure 7 (*a-j*). The C_p distributions display a distinct plateau typically associated with the LSBs are shown in Figure 6(b, Top: ①,②, and ③), and the pressure hump/crest near the quarter-chord region is the result of strong vortex roll-up. Furthermore, a pressure plateau can be found along the chordwise around 0.025<x/c<0.1, which corresponds to the laminar portion of the separation bubble. The distance between the transition location and the reattachment location[37] indicates the turbulent portion of the bubble. At 10° of incidence, the C_p distribution shows two peaks and one valley in between, which right behind the existing pressure plateau, indicating two clockwise vortices paired with a counter-clockwise rotating vortex shown in Figure 7(*g,* first column). In particular, a sudden jump in C_l followed with reduced amplitude oscillation around moderate angles of attack (from 10° to 14°) was observed during the pitching-up motion, see Figure 6 (a). This phenomenon was not discussed or explained before. However, by associating this with the change and development of the LSBs. Such lift oscillation is mainly due to the vortex-merging process occurred inside the LSBs around this incidence, leading to a very low-pressure vortex which enriches the circulation strength and resulting in a highly-damped oscillation in the lift coefficients. In particular, vorticity levels are highest at the leading-edge. The shear layer rolls up after separation, forming a primary, clock-wise rotating vortex. The clockwise vortex keeps growing and brings high-speed fluid towards the wall, which leads to the reattachment, as shown in Figure 7 (*a-f*). The convective velocities in the flow promote a vortex-merging process from *g* to *j* in Figure 7. Notable spatially periodic fluctuations develop in the separated shear layer further downstream are shown in Figure 7 (*g-j*, third column: trailing-edge vortices). These periodic disturbances are amplified and lead to vortical structures that shed in the wake region.

At Reynolds number 60,000, a good agreement on steady case comparison results between numerical and experimental are shown in Figure 8. By a closer examination of both steady numerical and experimental lift curves (circular and square markers, respectively), a sudden jump (change of the slope)

can be observed at an incidence of about 5° in both the simulation[25] and the measurement by Pelletier and Mueller[38]. Compared to the steady case around 5°, however, a similar but more significant perturbation on lift coefficient for pitching-up motion case is found at a delayed incidence of 7.85°, and accompanied by a low-damped oscillation on lift curve, see Figure 8 (a, with zoomed-in C_l plot: ① to ⑥). By examination at the flow field structure, in contrast to vortex-merging in the LSBs for Reynolds number at 30,000, a stabilized separation bubble is captured at Reynolds number of 60,000, which a single and large separation bubble structure is clearly shown in Figure 9 (*a-g*). A separation bubble with similar structures and development process was also confirmed by other investigators at various Reynolds numbers, regardless of whether the bubble is formed over a flat plate subjected to an adverse pressure gradient or an airfoil[39]. The pressure distribution can also confirm the trend of the LSBs development trend for Reynolds number of 60,000 in Figure 8 (b), which shows a reduced length on pressure plateau with increased value on suction force. Thus, a general indication is that the bubble reduces in size when the angle of attack increases, resulting in a perturbation on the lift coefficient.

The lift coefficient curve shows similar damped oscillations in the range of moderate angles of attack between Reynolds number of 30,000 and 60,000. At Reynolds number of 30,000, the vortex-merging in the separation bubble is captured and completed at the incidence of 10.3°. The C_l shows a significant jumped value. Then, at the Reynolds number of 60,000, no vortex-merging phenomenon is found in the separation bubble. In contrast, the oscillated lift coefficient exists around moderate incidences at Reynolds number of 30,000, and the process on the merger of vortices within the LSBs may play a central role. In regard to the free shear layer, vortex centers begin to approach each other due to the size of vortex cores exceeding the critical proportion of vortex spacing. The core finally merges to form a single merged-vorticity structure, which continues to expand as incidence increases. The consecutive merging of vortex pairs produces larger vortices. Eventually, the vorticity contained in each structure is continuously redistributed, leading to the formation of oscillated lift coefficients.
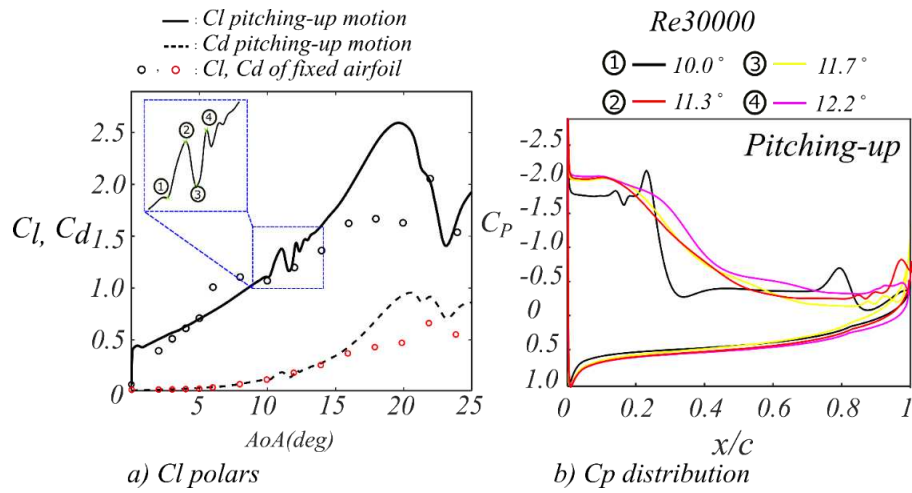
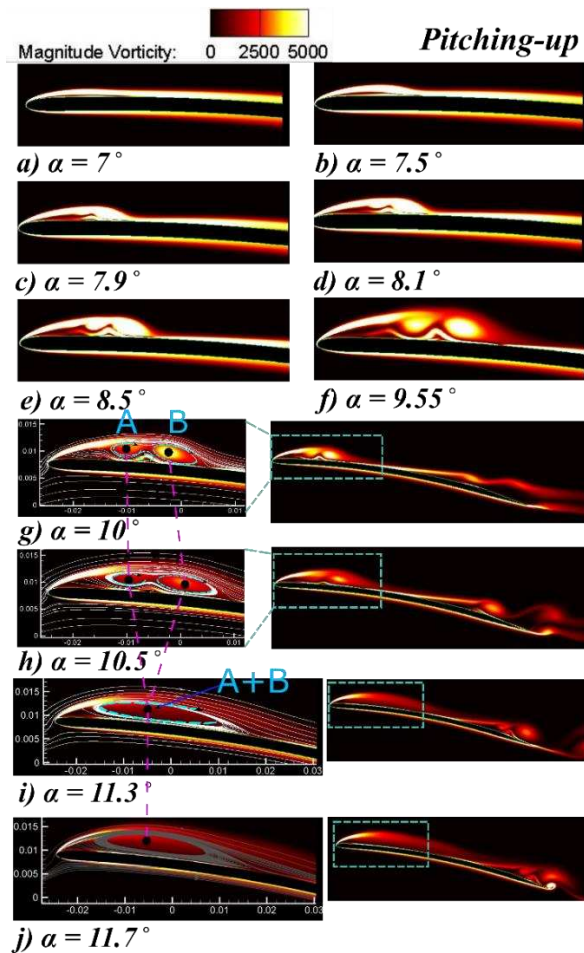Figure 6 Coefficients of (a) aerodynamic and (b) pressure obtained from a pitching airfoil at Re=30,000

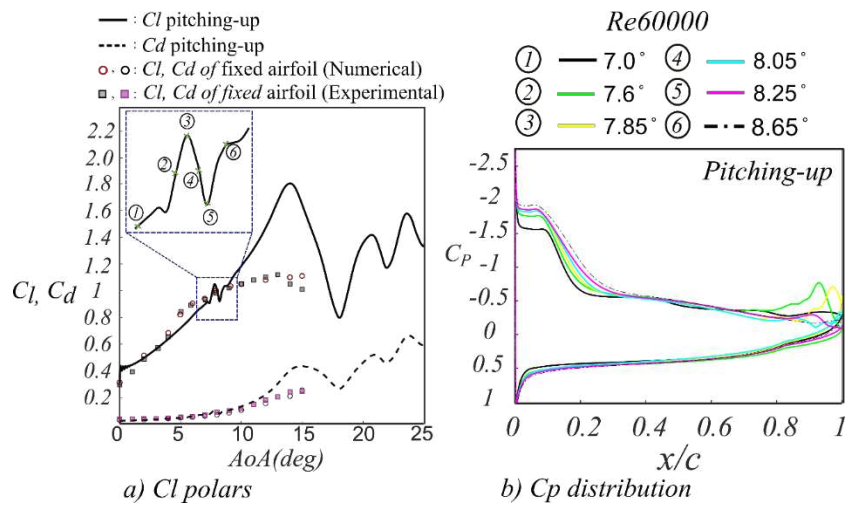Figure 7 Laminar separation bubble formation and evolution process (Re = 30,000)

a) Cl polars

b) Cp distribution

Figure 8 Coefficients of (a) aerodynamic and (b) pressure obtained from a pitching-up airfoil at

Re=60,000

a) $\alpha = 7°$

b) $\alpha = 7.6°$

c) $\alpha = 7.85°$

d) $\alpha = 8.05°$

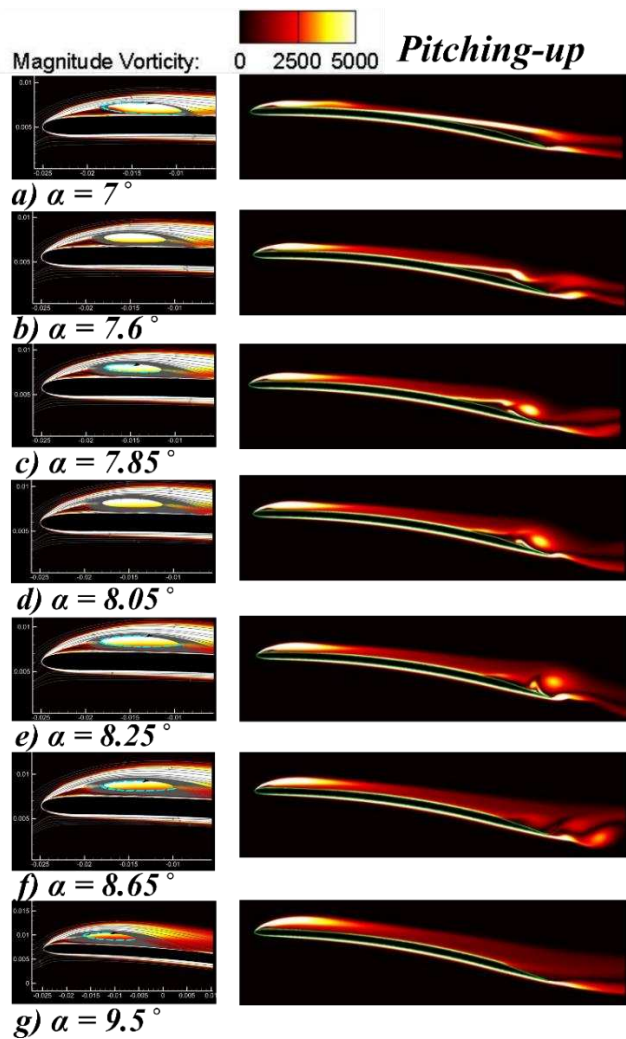e) $\alpha = 8.25°$

f) $\alpha = 8.65°$

g) $\alpha = 9.5°$

Figure 9 Laminar separation bubble formation and evolution process (Re = 60,000)

3.2.2 Flow categories for a pitching motion airfoil

In this section, the separation, transition, and reattachment location are based on a time-averaged pitching-up motion for the dynamic cases. For airfoils in fixed incidences, an earlier vortex roll-up introduces an upstream shift of transition, yielding a contraction on the laminar portion length of the bubble at higher angles of attack. However, during the airfoil in pitching-up motion, the large-scale vortices quickly break up into much smaller eddies (evidenced by a steeper pressure recovery in Figure 6, b), extending the streamwise area for which they can influence the dynamics of the flow. Consequently, lead to a continued increase of the distance between transition and reattachment even at high angles of attack, shown in Figure 10 (a, 11° to 14°), and Figure 10 (b, 8° to 11°). Through careful observation for the airfoil in the pitching-up motion, the turbulent portion of the separation bubble changes more significantly than the laminar part at both Reynolds numbers, which confirms the above points, shown in Figure 10 (a and b, at moderate incidences).
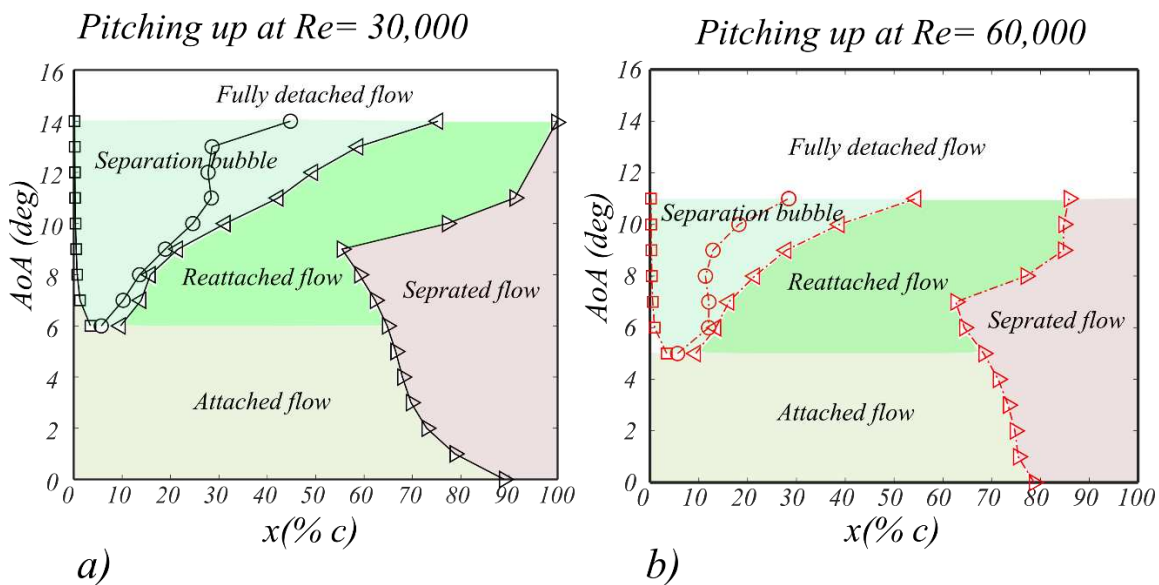

Figure 10 Bubble characteristics in pitching-up motion: Laminar separation loci: (—□—); Transition loci: (—○—);

Reattachment loci: (—◁—); Trailing-edge separation loci: (—▷—)

3.2.3 Flow field structure categories

Continue the discussion by taking a closer look into flow structures, including a well-defined leading-edge separation bubble associated with the nominally two-dimensional cambered-thin airfoil. The rapid formation and evolution of the LSBs in a pitching motion is well captured for Reynolds numbers of 30,000 and 60 000, respectively, as shown in Figure 11. To help understanding, flow categories for an airfoil in pitching-up motion that corresponding to incidences is classified in the following stages: attached flow with a limited region of trailing-edge separation (stage ①, at low angles of attack); Bubble formation and change (stage ②, at moderate angles of attack); Bubble bust and vortical flow formed (stage ③, moderate to high incidences); Fully separated flow (stage ④, at high incidences). The flow field undergoes different flow phenomena in a full cycle of the pitching-up motion demonstrated in the following:

Attached flow with a limited trailing-edge separation region (at stage ①): at low incidence, beginning the pitching-up motion, flow attached to the airfoil surface except a narrow separation region near the trailing-edge at low incidences for both Reynolds number. However, such separation region is clearly inhibited at higher Reynolds number. A slightly larger separation region is found near the trailing-edge and extended toward the leading-edge during its pitching-up movement at Reynolds number is 30,000. While at Reynolds number is 60,000, what is minimal? Change to insignificant ? trailing-edge separation region is observed. The unsteady flow structures are clearly shown in the near wake region, and the vortices shed alternatively from the upper separated boundary layer and the lower shear flow evolving from the trailing-edge. The unstable waves eventually develop into alternatively shed Von Karman type vortices in the far downstream region.

The formation and evolution of LSBs (i.e., stage ② to ③): the laminar separation bubble with entirely different shapes are formed at the airfoil leading-edge during the pitching-up movement for both Reynolds number from moderate to high angles of attack, see stage ② to ③ in Figure 11 (a and b). The formation of LSBs is due to the increase of momentum exchange from laminar to turbulent transition in the separated

shear layer, and the turbulence intensity is considerably increased after the LSBs. At the Reynolds number of 30,000, the vortex-merging phenomenon was found in the LSBs. Accompanied by such merging, a longer and thicker bubble is formed near the leading-edge during the airfoil further pitched up from 8° to 10° angles of attack, see stage ② in Figure 11 (a). As further upstroke to 10.5°, vortex starts to generate at the rear part of the separation bubble before being released downstream marked as V_1 and V_2. The vortex keeps developing as the incidence increases, which begins to be convected downstream during its shedding sequential- increasing their length and the vorticity magnitude, visible in Figure 11 (a), marked as V_3 and V_4. It wrapped around the upstream and downstream vortices, forming an S-shape paired-vortices, namely the 'braid region' between vortices[40], just upstream of the downstream traveling vortex. The LSBs further expanded in size and traveled towards the trailing-edge of the airfoil as incidence increased. Finally, a long bubble has formed with over approximately half of the suction surface, shown in stage ③. At Reynolds number of 60,000, a relatively flat separation bubble with no vortex-merging is observed. The bubble thickness changes less obviously than that at the Reynolds number of 30,000. In contrast, a rapid breakdown to smaller scales vortices in the trailing-edge region between 7.55° and 8.5° angles of attack in Figure 11 (b) stage ②.

Stalling process (i.e., between stage ③ and ④): the LSBs progressively lengthens and covers the entire airfoil leading to the occurring of a thin airfoil stall. At Reynolds number of 30,000, the large vortex is strengthening and causing higher aerodynamic loads before the stall, which presents a sudden rise in the lift-curve slope between α = 16° and 20° as evidenced in Figure 6 (a). The adverse pressure gradient becomes too high, which leads to the separated shear layer fails to re-attach, resulting in an abrupt forward propagation of flow reversal to the leading-edge. As the incidence continues to rise, a trailing-edge vortex and subsequent induction of a strong reverse flow between the two counter-rotating vortices that ultimately tear them apart, see Figure 11 (a, at stage ④) between α = 23° and 25°. For Reynolds number of 60,000, the stall occurs at angles of attack of 15° which is earlier than at a Reynolds number of 30,000. After the

stall, the leading-edge vortex grows in size and then leaves the suction surface, and a dynamic stall occurs when the lift reaches its maximum value. The subsequent motion of the dynamic stall vortex is a principal contributor to the airfoil lift and drag variation shown in Figure 8 (a).
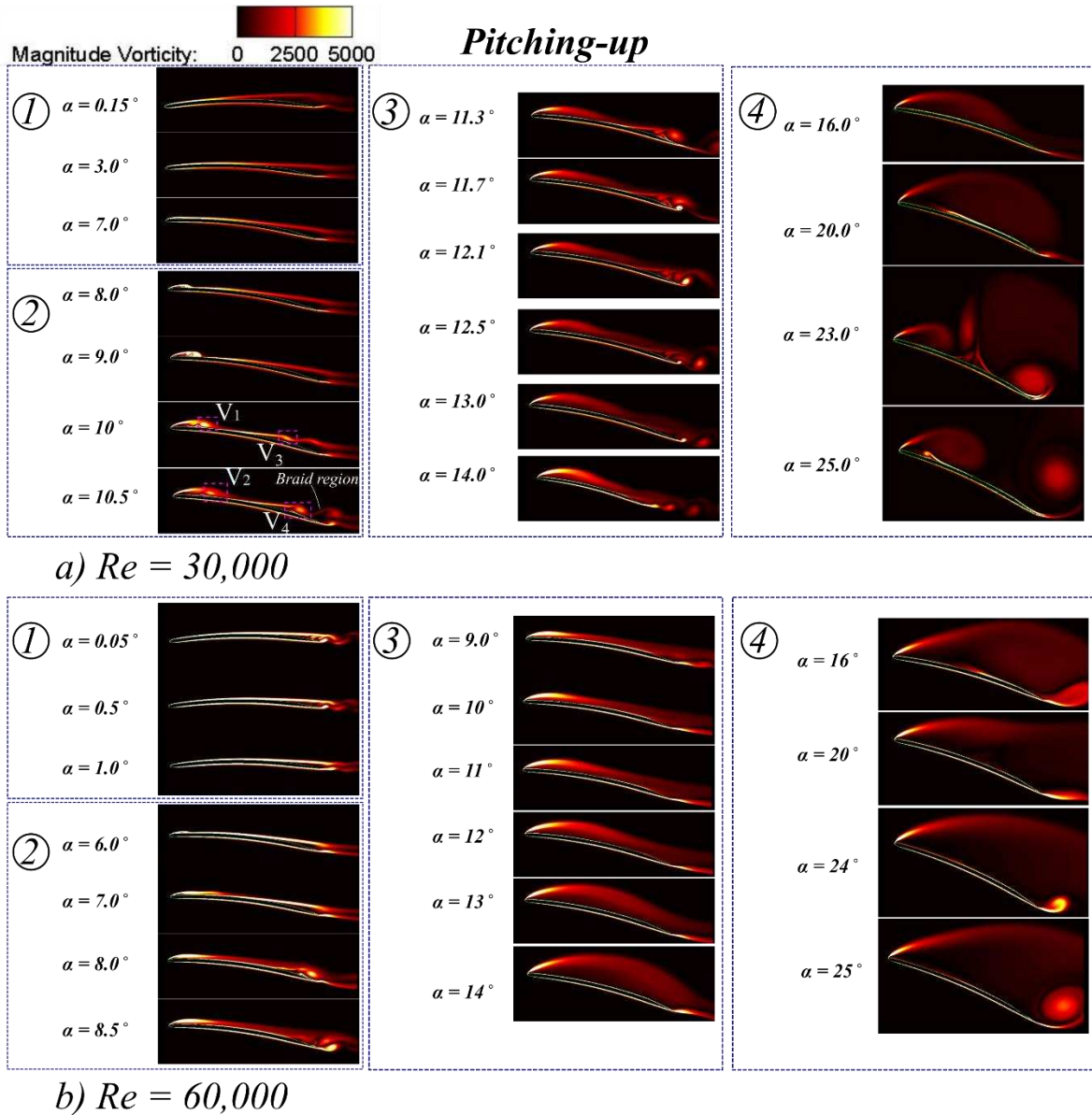

Figure 11 Flow field structure for pitching-up airfoils

4. Conclusion

The prediction of transitional flows over a pitching-up motion cambered-thin airfoil under low-Reynolds-number conditions has been investigated through an unsteady Reynolds Averaged Navier-

Stokes (URANS) solution implemented with the $k - \omega$ SST $\gamma - \widetilde{Re}_{\theta t}$ turbulence-transition model.. For the fixed airfoil, short LSBs form near the leading-edge. The LSBs' length increased as the incidence rises, moving the transition location toward the leading-edge and the reattachment point toward the trailing-edge.

In the cases of the dynamic airfoil, the flow field undergoes different flow phenomena during pitching-up motions. The upper surface is dominated by the trailing-edge separation at low incidences between $0°$ and $7°$ for both Reynolds numbers. With further pitching up, LSBs start to form near the leading-edge. The dynamic characteristics of such LSBs associated with the perturbation on aerodynamic lift are clearly shown, where significant differences in amplitude are found for the two different Reynolds numbers. Vortex breaking up and merging are transpired? What do you want to say? inside the laminar separation bubble at the lower Reynolds number, resulting in a more significant perturbation on the lift. However, for the higher Reynolds number, the LSBs show a different behavior, and therefore less prominent. During the pitching-up motion, the separation locations move towards the leading-edge more quickly. Within the LSBs, the transition also moves downstream. During the pitching motion, the laminar separation, transition, and turbulent reattachment shows an increase in the length of LSBs with the growth of incidences. For the higher Reynolds number, the size of LSBs is much smaller.

Appendix

Notation

AoAs, α	Angle of Attack
$\dot{\alpha}$	dimensionless pitch rate
c	chord length
C_f	Skin friction coefficient
C_p	Pressure coefficient

C_L, C_l	Three-, two dimensional lift coefficient
C_D, C_d	Three-, two dimensional drag coefficient
Re_c	Chord Reynolds number
T_i	free stream turbulent intensity
Δt	Time step size
U_∞	freestream velocity
x_{sep}/c	Non-dimensional separation location
x_{tr}/c	Non-dimensional transition location
$x_{reattch}/c$	Non-dimensional reattachment location

Acknowledgments

5. References

1 Gaster M. The Structure and Behaviour of Laminar Separation Bubbles. *Reports and Memoranda No 3595*. 1969.

2 Gupta R, Ansell PJ. Unsteady Flow Physics of Airfoil Dynamic Stall. *AIAA Journal*. 2019; 57: 165-75.

3 Shimoyama K, Kamisori K. Study of Aerodynamic and Heat-Exhaust Characteristics for a High-Altitude Long-Endurance Unmanned-Aerial-Vehicle Airfoil. *Journal of Aircraft*. 2017; 54: 1317-27.

4 Anyoji M, Nonomura T, Aono H, et al. Computational and Experimental Analysis of a High-Performance Airfoil Under Low-Reynolds-Number Flow Condition. *Journal of Aircraft*. 2014; 51: 1864-72.

5 Zhong J, Li J, Guo P, Wang Y. Dynamic stall control on a vertical axis wind turbine aerofoil using leading-edge rod. *Energy*. 2019; 174: 246-60.

6 Mueller TJ, DeLaurier JD. Aerodynamics of Small Vehicles. *Annual Review of Fluid Mechanics*. 2003; 35: 89-111.

7 Dovgal A, Kozlov V, Michalke A. Laminar boundary layer separation: Instability and associated phenomena. *Progress in Aerospace Sciences*. 1994; 30: 61-94.

8   Lambert AR, Yarusevych S. Characterization of Vortex Dynamics in a Laminar Separation Bubble. *AIAA Journal*. 2017; 55: 2664-75.

9   Michelis T, Yarusevych S, Kotsonis M. Response of a laminar separation bubble to impulsive forcing. *Journal of Fluid Mechanics*. 2017; 820: 633-66.

10   Tani I. Low Speed Flow Involving Bubble Separation. *Progress in Aerospace Sciences*. 1964; 5: 70-103.

11   Horton HP. Laminar Separation Bubbles in Two and Three Dimentional Iincompressible Flow. *Department of Aeronautical Engineering*. London: Queen Mary College, 1968.

12   Westini KJA, Boiko AV, Klingmanni BGB, Kozlov VV, Alfredsson PH. Experiments in a boundary layer subjected to free stream turbulence-Part 1 Boundary layer structure and receptivity. *Journal of Fluid Mechanics,.* 1994; 281: 193-218.

13   O'Meara MM, Mueller TJ. Laminar Separation Bubble Characteristics on an Airfoil at Low Reynolds Numbers. *AIAA Journal*. 1987; 25: 1033-41.

14   DeMauro EP, Dell'Orso H, Zaremski S, Leong CM, Amitay M. Control of Laminar Separation Bubble on NACA 0009 Airfoil Using Electroactive Polymers. *AIAA Journal*. 2015; 53: 2270-9.

15   Rinoie K, Komuro T, Nakamura Y, Sunada Y. Airfoil Stall Suppression Using Feedback-Controlled Rectangular Bubble-Burst Control Plate. *Journal of Aircraft*. 2015; 52: 353-7.

16   Sudhakar S, Karthikeyan N, Suriyanarayanan P. Experimental Studies on the Effect of Leading-Edge Tubercles on Laminar Separation Bubble. *AIAA Journal*. 2019; 57: 5197-207.

17   Lee D, Nonomura T, Oyama A, Fujii K. Comparison of Numerical Methods Evaluating Airfoil Aerodynamic Characteristics at Low Reynolds Number. *Journal of Aircraft*. 2015; 52: 296-306.

18   Bernardos L, Richez F, Gleize V, Gerolymos GA. Algebraic Nonlocal Transition Modeling of Laminar Separation Bubbles Using k−ω Turbulence Models. *AIAA Journal*. 2019; 57: 553-65.

19   Langtry RB, Menter FR. Correlation-Based Transition Modeling for Unstructured Parallelized Computational Fluid Dynamics Codes. *AIAA Journal*. 2009; 47: 2894-906.

20   Suluksna K, Juntasaro E. Assessment of intermittency transport equations for modeling transition in boundary layers subjected to freestream turbulence. *International Journal of Heat and Fluid Flow*. 2008; 29: 48-61.

21   Dick E, Kubacki S. Transition Models for Turbomachinery Boundary Layer Flows: A Review. *International Journal of Turbomachinery Propulsion and Power*. 2017; 2: 4.

22   Liu J, Xiao Z, Fu S. Unsteady Transition Studies over a Pitching Airfoil Using a k-ω-γ Transition Model. 2018; 56: 3776-81.

23   Geng F, Kalkman I, Suiker ASJ, Blocken B. Sensitivity analysis of airfoil aerodynamics during pitching motion at a Reynolds number of 1.35×10^5. *Journal of Wind Engineering and Industrial Aerodynamics*. 2018; 183: 315-32.

24   Choudhry A, Arjomandi M, Kelso R. A study of long separation bubble on thick airfoils and its consequent effects. *International Journal of Heat and Fluid Flow*. 2015; 52: 84-96.

25   Chen ZJ, Qin N, Nowakowski AF. Three-Dimensional Laminar-Separation Bubble on a Cambered Thin Wing at Low Reynolds Numbers. *Journal of Aircraft*. 2012; 50: 152-63.

26   Counsil JNN, Boulama KG. Low-Reynolds-Number Aerodynamic Performances of the NACA 0012 and Selig–Donovan 7003 Airfoils. *Journal of Aircraft*. 2013; 50: 204-16.

27   Catalano P, Tognaccini R. Turbulence Modeling for Low-Reynolds-Number Flows. *AIAA Journal*. 2010; 48: 1673-85.

28   Menter FR, Langtry RB, Likki SR, Suzen YB, Huang PG, Volker S. A Correction-Based Transition Model Using Local Variables- Part I: Model Formulation. *Journal of Turbomachinery*. 2006; 128: 413-22.

29   Lee T, Gerontakos P. Investigation of flow over an oscillating airfoil. *Journal of Fluid Mechanics*. 2004; 512: 313-41.

30   Kim Y, Xie Z-T. Modelling the effect of freestream turbulence on dynamic stall of wind turbine blades. *Comput Fluids*. 2016; 129: 53-66.

31   Wang S, Ingham DB, Ma L, Pourkashanian M, Tao Z. Turbulence modeling of deep dynamic stall at relatively low Reynolds number. *J Fluid Struct*. 2012; 33: 191-209.

32   Gharali K, Johnson DA. Dynamic stall simulation of a pitching airfoil under unsteady freestream velocity. *J Fluid Struct*. 2013; 42: 228-44.

33   Barnes CJ, Visbal MR. Stiffness effects on laminar separation flutter. *J Fluid Struct*. 2019; 91: 102767.

34 Coleman GN, Rumsey CL, Spalart PR. Numerical study of turbulent separation bubbles with varying pressure gradient and Reynolds number. *Journal of Fluid Mechanics*. 2018; 847: 28-70.

35 Lian Y, Shyy W. Laminar-Turbulent Transition of a Low Reynolds Number Rigid or Flexible Airfoil. *AIAA Journal,*. 2007; 45: 1501-13.

36 Lei J, Liu Q, Li T. Suction control of laminar separation bubble over an airfoil at low Reynolds number. 2019; 233: 81-90.

37 Marxen O, Henningson DS. The effect of small-amplitude convective disturbances on the size and bursting of a laminar separation bubble. *Journal of Fluid Mechanics*. 2011; 671: 1-33.

38 Pelletier A, Mueller TJ. Low Reynolds Number Aerodynamics of Low-Aspect-Ratio, Thin/Flat/Cambered-Plate Wings. *Journal of Aircraft*. 2000; 37: 825-32.

39 Almutairi J, ElJack E, Alqadi I. Dynamics of laminar separation bubble over NACA-0012 airfoil near stall conditions. *Aerospace Science and Technology*. 2017; 68.

40 Williamson CHK. Vortex Dynamics in the Cylinder Wake. *Annual Review of Fluid Mechanics,*. 1996; 28: 477-539.